Scripta Materialia 245 (2024) 116049

Contents lists available at ScienceDirect

Scripta Materialia

journal homepage: www.journals.elsevier.com/scripta-materialia

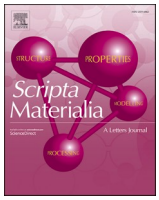

New insights into the character of austenite-ferrite boundaries in an additively manufactured duplex stainless steel

N. Haghdadi [a,*], A.J. Breen [b,c], H. Chen [b,c], F. Theska [b], W.J. Davids [b,c], X.Z. Liao [b,c], G.S. Rohrer [d,#], S.P. Ringer [b,c], S. Primig [a,*]

[a] School of Materials Science & Engineering, UNSW Sydney, Sydney, NSW 2052, Australia
[b] Australian Centre for Microscopy & Microanalysis, The University of Sydney, Sydney, NSW 2006, Australia
[c] School of Aerospace, Mechanical and Mechatronic Engineering, The University of Sydney, Sydney, NSW 2006, Australia
[d] Department of Materials Science and Engineering, Carnegie Mellon University, Pittsburgh, PA, 15213-3890, USA

ARTICLE INFO

Keywords:
Interphase boundary
Segregation
Crystallography
Duplex stainless steel

ABSTRACT

The crystallography and chemistry of interfaces between austenite and ferrite in duplex steels control many important materials properties but remain poorly understood. In this study, we experimentally show that in an additively manufactured and heat treated duplex stainless steel, the majority of austenite-ferrite interfaces terminate on $\{111\}_A/\{110\}_F$ planes, and this behaviour is more pronounced for rational interfaces with the Kurdjomov-Sachs orientation relationship. Interface segregation was found to be controlled by not only the interface crystallography but also the bonding properties of solute atoms. Solute elements showed higher interfacial excess at irrational interfaces. Furthermore, a heterogeneous distribution of selected solute elements in austenite-ferrite interfaces planes was observed. Our findings reinforce the importance and, in fact, necessity to consider five independent crystallographic parameters and chemical architecture of interphase boundaries for advanced control of mechanical and other critical properties in duplex materials.

The interphase boundary character in duplex materials determines many intergranular phenomena such as sensitization [1], pitting [2], and cracking [3], and in turn, plays a significant role in controlling the mechanical and corrosion properties of engineering parts. The extent to which properties are related to the interphase boundary character depends not only on boundary's crystallography, but also on the solute architecture at the boundary versus in either neighbouring grain (segregation). This has driven the development of interface engineering approaches where advanced properties have been achieved via manipulating the structure, crystallography, and chemistry of interfaces [4–8]. The development of advanced techniques to characterize all of these characteristics is a critical enabler for interface engineering. However, challenges exist in the full characterization of interfaces due to their five crystallographic degrees of freedom and the atomic-scale heterogenous segregation (non-random distribution) of solute elements at the interface.

The five crystallographic parameters defining an interface include parameters describing the misorientation angle/axis and the habit plane between the two adjacent grains [9]. These parameters determine the free volume at the boundary, the atomic arrangement (coherence), and the energy of the interface. Properties such as solute segregation [10], interface sliding [11], slip transition [12], and precipitation propensity [13] are strongly linked to the crystallography of interfaces. While the misorientation angle/axis of interfaces is accessible via straightforward 2D electron backscatter diffraction (EBSD), the characterization of habit planes requires 3D crystallographic analyses from e.g., 3D EBSD, high-energy X-ray and transmission electron microscopy (TEM). All of those are time-consuming and costly. Alternatively, a stereological method, originally developed by Rohrer et al. [14], can be used to predict the average expected habit plane across populations of boundaries from EBSD data with $>$ 95% accuracy but this does not provide crystallographic habit plane information on an individual boundary.

In addition to the crystallography, the solute architecture at the interface can significantly impact various properties of interfaces including lattice misfit [15], energy (Gibbs adsorption) [16], local kinetics (solute drag) [17], mechanical properties [18], and phase

* Corresponding authors.
E-mail addresses: nima.haghdadi@unsw.edu.au (N. Haghdadi), s.primig@unsw.edu.au (S. Primig).
Greg Rohrer was an Editor of the journal during the review period of the article. To avoid a conflict of interest, Greg Rohrer was blinded to the record and another editor processed this manuscript.

https://doi.org/10.1016/j.scriptamat.2024.116049
Received 22 January 2024; Received in revised form 15 February 2024; Accepted 18 February 2024
Available online 20 February 2024
1359-6462/© 2024 The Author(s). Published by Elsevier Ltd on behalf of Acta Materialia Inc. This is an open access article under the CC BY license (http://creativecommons.org/licenses/by/4.0/).

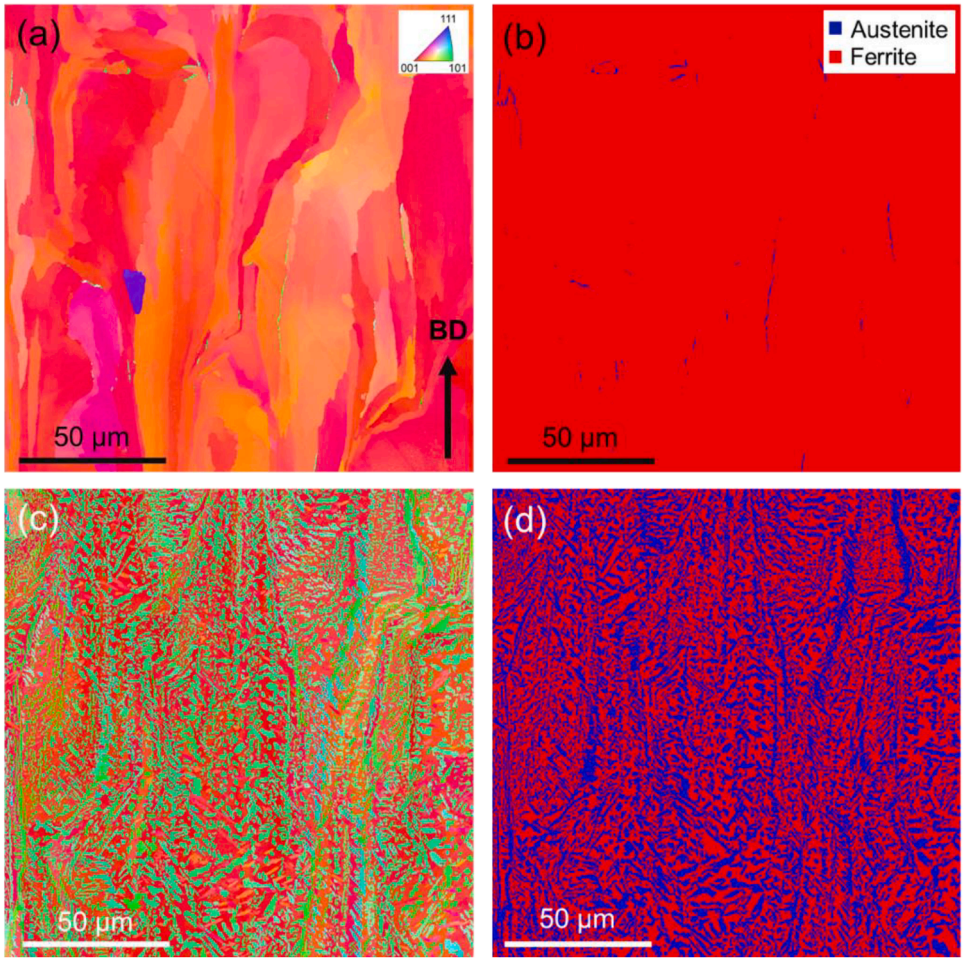

Fig. 1. EBSD maps of laser powder bed fusion processed DSS in the (a,b) as-built and (c,d) heat treated (10 min at 1000 °C) conditions. Inverse pole figure maps (a,c) are coloured with respect to the build direction (BD). In the phase maps (b,d) red and blue denote ferrite and austenite, respectively.

transformations [19]. Therefore, incorporating solute segregation into interface characterization is essential. Atom probe tomography (APT) is the perhaps most powerful technique capable of revealing such information where the position and chemical identity of atoms across an interface can be reconstructed in 3D with sub-nm resolution. Although some progress in crystallographic/chemical interface characterization using APT and correlative techniques has been made in single phase alloys [20–23], the current understanding of the segregation at the interphase boundaries and its link to the crystallography in duplex materials remains poor.

Duplex stainless steel (DSS) is a common example of an alloy with a duplex microstructure that is composed of almost equal fractions of austenite and δ−ferrite (ferrite in the following) when in equilibrium. DSS offers advanced mechanical and corrosion properties and is a material of choice for critical applications in harsh environments such as underwater infrastructure and heat exchangers [24]. It has been recently shown [25–30], that DSS can be processed by additive manufacturing (AM), although a post-AM heat treatment is typically needed to achieve a ~50–50 austenite-ferrite microstructure. Further, it has been shown that as-built AM DSS suffers from non-equilibrium grain and interphase boundary segregation of elements such as Cr, which is readily eliminated via the post-AM heat treatment [25,27]. Notably, this 'regained equilibrium' microstructure is usually finer than in wrought counterparts, and has been reported to have an attractive property profile including a great combination of strength/ductility [27] and corrosion resistance [26,28], comparable or even superior to its wrought counterpart. Generally, many important properties of DSS are expected to strongly depend on the crystallography and chemistry of austenite-ferrite interfaces [2,3,11–13]. From a fundamental point of view, the post-AM annealed microstructure of DSS is an ideal candidate to establish the currently missing link between the austenite-ferrite interface crystallography and chemistry. From a technological point of view, advanced understanding of the chemical/crystallographic interphase boundary characteristics will pave the way towards engineering these microstructural features in AM processed duplex materials to unlock advanced properties.

Duplex stainless steel (DSS 2205) powder with the composition (in wt%) of 22.60 Cr, 5.90 Ni, 3.20 Mo, 1.10 Mn, 0.02C, 0.60 Si, 0.18 N, 0.02 P, 0.01 S, and a balance of Fe was acquired from Sandvik. Cubic samples of $5 \times 15 \times 15$ mm^3 were printed using laser powder bed fusion (LPBF), with details given in [25]. To achieve a ~50/50 austenite-ferrite fraction and remove non-equilibrium grain boundary segregation, these samples were subsequently heat treated for 10 min at 1000 °C as elaborated in [25,27]. EBSD and stereological analyses were carried out as detailed in [14,25]. APT tips were lifted out from site-specific locations using a Thermofisher G4 Hydra Plasma focused ion beam (FIB)-SEM from the mid height of the AM samples. APT measurements were carried out using a CAMECA Local Electrode Atom Probe (LEAP) 4000X Si with details given in [25]. Interfacial excess mapping was carried out using the MATLAB® atom probe toolbox [31]. The original interface triangulation method [32] was modified using a coarse Delaunay triangulation to improve counting statistics for each face of the interface and mitigate artefacts from APT acquisition.

The as-built microstructure of DSS 2025 is predominantly ferritic

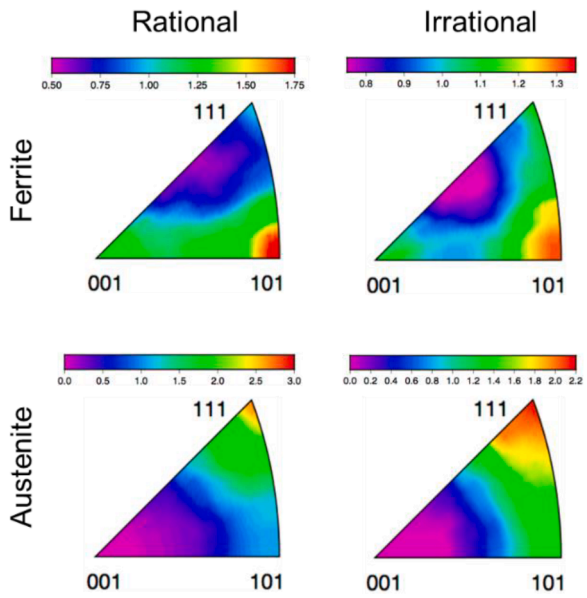

Fig. 2. Habit plane distributions for rational and irrational interfaces in the ferrite and austenite crystal frames. Colour keys show multiples of random distribution (MRD).

with most of ferrite grains exhibiting a columnar morphology and a sharp ⟨100⟩ fibre texture (Fig. 1). A small phase fraction of austenite (~2%) is observed with a predominantly allotriomorphic morphology precipitating along ferrite-ferrite grain boundaries. The predominance of ferrite, which is due to the high cooling rate during LPBF, necessitated a post-AM heat treatment to achieve a more balanced austenite-ferrite ratio [25]. During 10 mins heat treatment at 1000 °C, austenite forms both inter- and intragranularly (Fig. 1). The intragranular austenite islands (grains) are ~2 μm in diameter. The microstructure after the heat treatment consists of ~ 48 % austenite with a high tendency of individual grains to form rational (e.g., Kurdjomov-Sachs (K-S) and Nishiyama-Wasserman (N-W)) interfaces with their parent ferrite grains [25]. K-S is found to be the most dominant orientation relationship (OR). Therefore, for further analysis, interfaces are classified into two groups of K-S (rational) i.e., those with ≤10° from the ideal K-S OR, and non-K-S (irrational). It was found that ~81% of the total length of all interfaces are rational.

The formation and growth of austenite from ferrite at 1000 °C occurs via diffusion-controlled processes. Nuclei with minimum interfacial energy are preferred. Usually, rational interfaces minimize the nucleation activation energy as they contain a high number of atomic bonds [33]. The growth, however, occurs along irrational interfaces. This is because such interfaces have a limited number of atomic bonds, and the transformation is controlled by diffusion rather than structural constraints. This is the reason why austenite tends to grow into those ferrite grains to which it has an irrational OR [34].

Using the stereological analysis method [14], the austenite and ferrite habit plane distributions are calculated for both rational and irrational interphase boundaries (Fig. 2). For both types of interfaces, ferrite and austenite terminate mostly on {110} and {111} planes, respectively. For the rational interfaces, the intensity of {110} ferrite planes and {111} austenite planes are 1.7 and 3.0 multiples of random distribution (MRD), respectively. As expected, the intensity of the interphase boundary plane distributions in both ferrite and austenite is lower (1.3 and 2.2 MRD, respectively) for irrational interfaces, demonstrating a relatively lower tendency of these interphase boundaries to terminate on $\{110\}_F//\{111\}_A$. The higher tendency of rational interfaces to terminate on $\{110\}_F//\{111\}_A$ is because these interfaces are the ones formed during initial nucleation to minimize the interfacial energy. Interfaces with the lowest energy are formed when the closest-packed planes of each phase, i.e., {111} in austenite and {110} in ferrite, are parallel to each other [35].

To study the difference between rational and irrational interfaces in terms of their solute segregation behaviour, various typical interfaces

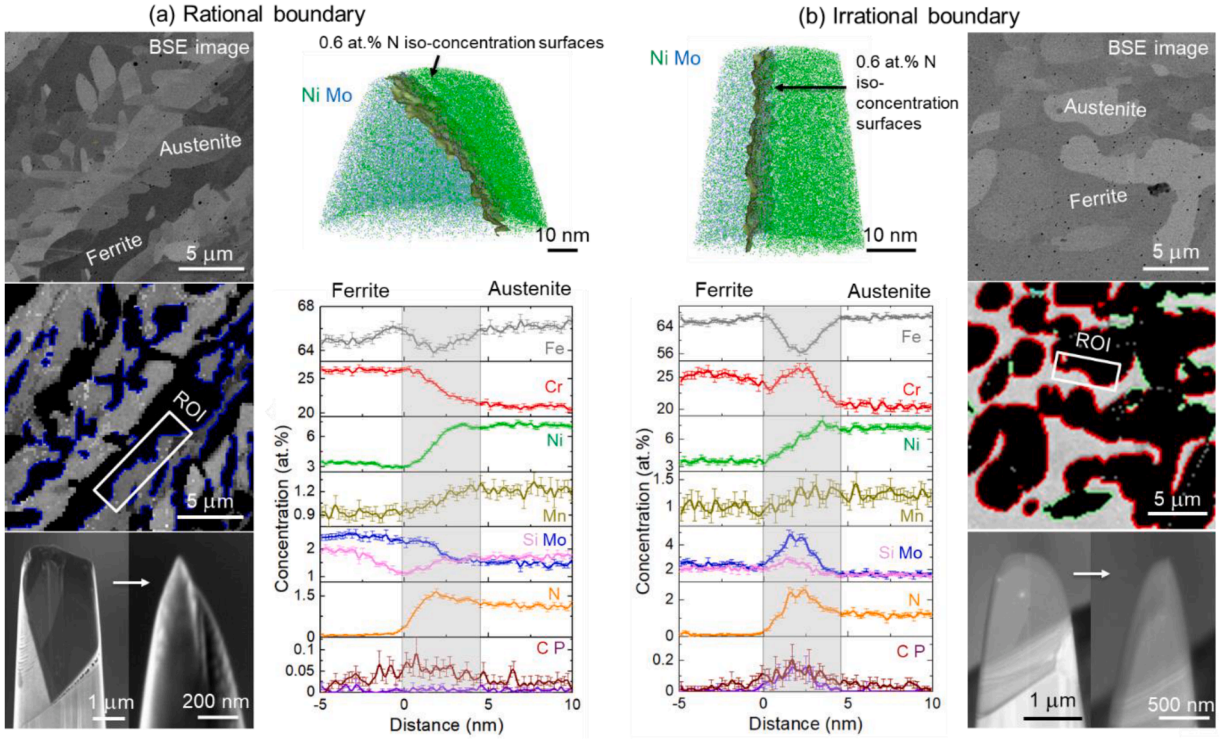

Fig. 3. Correlative SEM-EBSD-FIB assisted site-specific APT analysis of typical (a) rational and (b) irrational interphase boundaries in the heat-treated DSS. The blue and red lines in the EBSD maps correspond to the rational and irrational GBs, respectively.

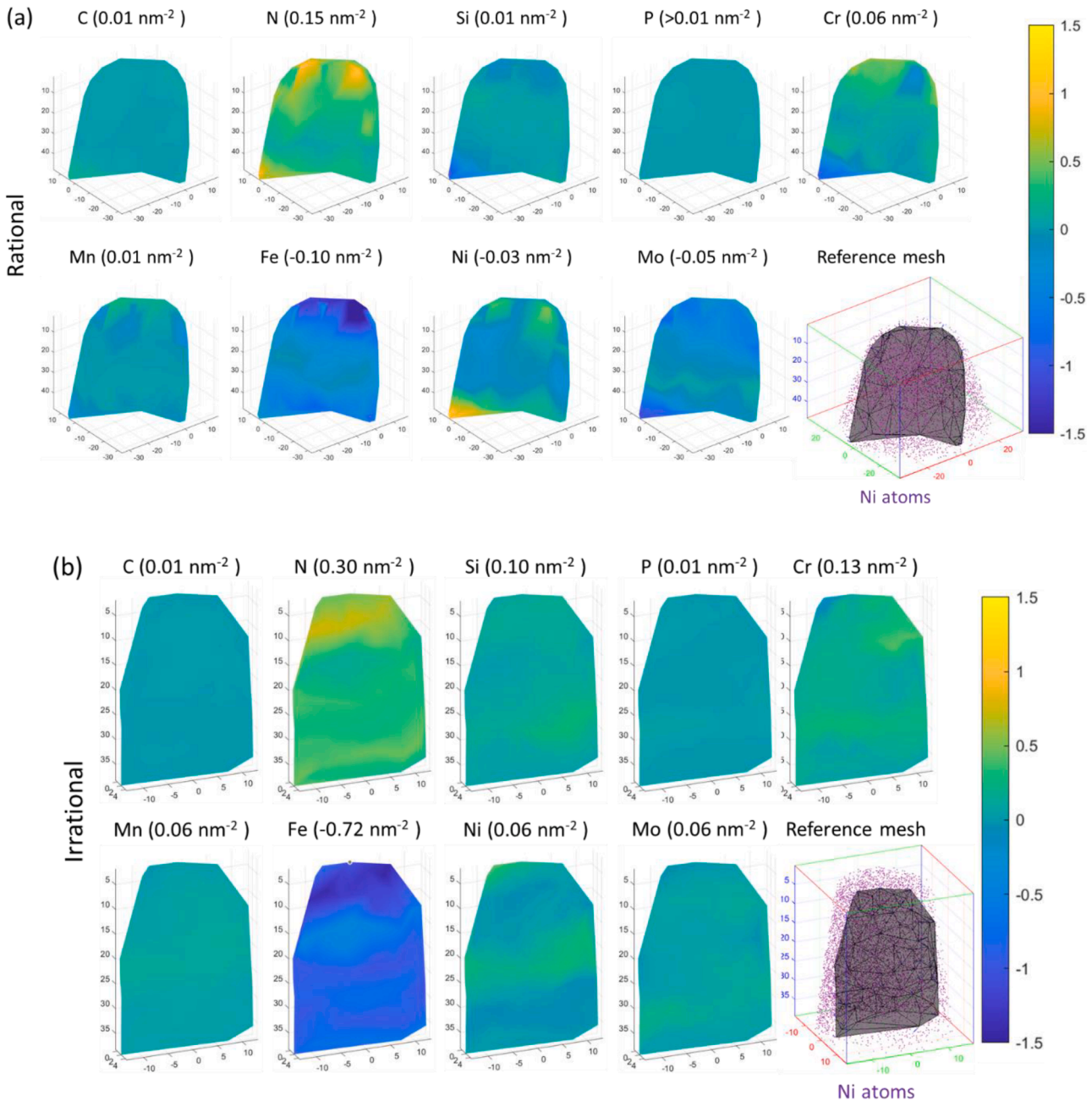

Fig. 4. Interfacial excess maps revealing heterogeneous solute distribution in the interface plane for rational versus irrational DSS interphase boundaries. Spatial dimensions are in nm, all excess is shown in nm^{-2}.The average interfacial excess across the boundary for each element is shown above each map.

were site-specifically lifted-out and studied via APT. As can be seen in Fig. 3a, Fe, Ni, Mn, and N partition into austenite, while Cr, Mo and Si partition into ferrite. A similar trend of solute partitioning between austenite and ferrite is observed for the irrational interface (Fig. 3b). As can be seen in the concentration profiles, the interface region spans across a ~ 5 nm wide region. Based on the Cahn-Hilliard model [36,37], the 'equilibrium' interface width and energy are determined by two competing contributions, i.e., the gradient energy and the barrier energy. Increases in either or both will result in a higher interface energy. A higher gradient energy alone will increase the width as steeper concentration gradients are higher energy propositions, while a higher barrier energy alone will decrease the width to reduce the amount of material contained in the higher energy interface. Further, any changes of the width from the equilibrium state will result in higher interfacial energy. However, it is to be noted that the diffuseness of the interfaces here may be observed as they may not be perfectly planar over the intercepted surface [38].

Although the partitioning of elements between the two phases is similar for the two types of interfaces studied, the interfacial segregation behaviour is significantly different as a function of interface coherence. This is important as the solute decoration of interfaces controls their cohesion. C and P usually have an embrittling effect while Cr is known to be strengthening element [39]. Other elements such as Al, Si and Fe may provide either cohesion or embrittlement as reported for various materials and interfaces, although to a minor extent [39]. In the current study, there are only minor peaks of C and N, and an obvious depletion in Fe in the concentration profiles of the rational interface (Fig. 3a). The overall segregation of solute elements is more pronounced at the irrational interface. As can be seen in Fig. 3b, significant peaks of Cr, Mo, Si, N, C and P can be observed in the concentration profiles of the irrational

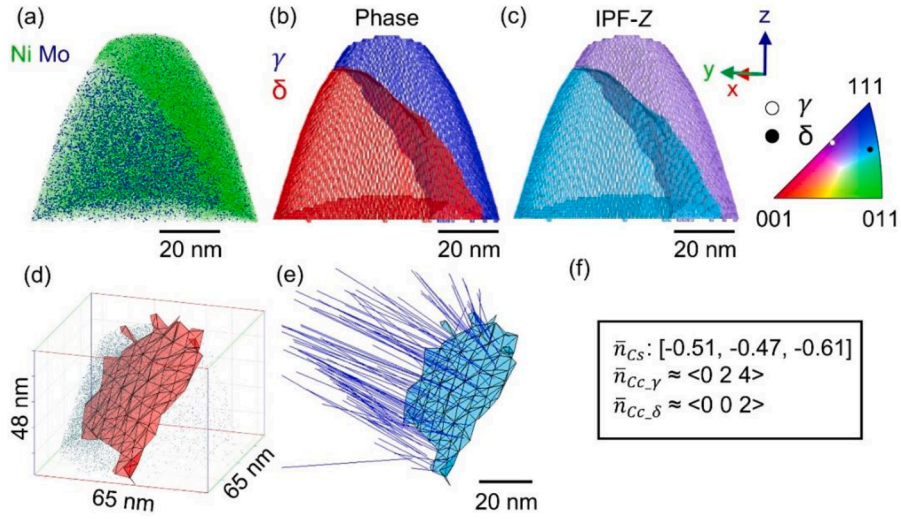

Fig. 5. (a) APT reconstruction of a rational interface showing Ni and Mo atoms. (b) Phase map showing austenite (γ) and ferrite (δ) grains. (c) Inverse pole figure map and corresponding colour key. (d) Isosurface mesh of austenite-ferrite interface. (e) Normal vectors of each isosurface mesh component from which an average surface normal was calculated. (f) Calculated average surface normal ($\bar{n}$) of the austenite-ferrite interface in the specimen frame of reference (Cs), austenite crystal frame (Cc_ γ) and ferrite crystal frame (Cc_ δ).

interphase boundary, indicative of pronounced segregation of these elements to the interface. Also, Fe shows a pronounced depletion at the interphase boundary. The observed limited interfacial segregation of elements at the rational interface is due in part to the high interfacial coherency and, therefore, low capacity to accommodate solute atoms [40]. It is also known that an irrational interface has a higher bonding energy and site density for segregation [41,42].

The extent to which elements segregate at individual interfaces is a function of the interface energy as well as the mixing tendency between the solute and the solvent atoms. To minimize their energy, interfaces adsorb solutes and impurity atoms [43]. Generally, a higher positive (or unfavourable) mixing enthalpy in the bulk and a larger negative value of enthalpy of segregation leads to a stronger driving force for phase separation and segregation to grain boundary [10]. Significant segregation of Mo to the ferrite/austenite boundary is due to its relatively high negative enthalpy of segregation to the ferrite/austenite interface [44]. C and P show similar segregation patterns, and this may be related to their almost similar enthalpies for segregation at grain boundaries in Fe [45]. There are reports showing that C segregation is mainly driven by the presence of Mn, whereby Mn segregation induces co-segregation of C [45]. This is, however, not significant in the present work as the extent of Mn segregation is much lower than that of C. The behaviour of Ni also deserves comment as only limited segregation is observed (Fig. 3). This is in line with previous studies on austenite-ferrite interfaces discussing that Mo, Mn and Si atoms have higher negative interfacial bonding energies than Cr and Ni [46]. Another interesting observation is the simultaneous segregation of Ni and Cr at the irrational interface. This contradicts a previous report [42] that these elements usually repel each other at interfaces i.e., Cr depletes where Ni segregates.

A more detailed analysis of the distribution of individual species across interfaces reveals that segregation and depletion of various elements does not occur evenly along the entire interface. To study this in detail, the Gibbsian excess is determined across individual segments of the interfaces using a method previously proposed in [32]. The tendency of a solute to segregate at an interface can be quantified using Gibbs adsorption isotherm through the so-called relative Gibbsian excess (or deficiency) [47]. The results show that all elements except C and P have a heterogeneous distribution in the interface plane across the reference mesh within the interface plane (Fig. 4). Interestingly, the coherency of the interface itself seems to have no impact on the degree of heterogeneity. There is a general similarity between the two types of interfaces where N, Si, Cr, Ni, and Mo seem to show a higher level of heterogeneity compared to C, P and Mn. Note that the average Gibbsian excess for C and P was negligible regardless of the type of interface. Similarly, N and Fe, versus Si and Cr exhibit repulsive versus attractive interactions at both types of interfaces, respectively. Ni and Mo exhibit strongly repulsive interaction across the rational interface, which is diminished across the irrational interface. These findings are important as they can significantly affect the precipitation, corrosion, and cracking properties of interfaces.

Analysis of crystallographic information directly from the APT datasets combined with correlative EBSD data acquired prior to lift-out of the APT specimens allows spatial calibration of the APT reconstructions and subsequent crystallographic characterisation of the interfaces collected. Fig. 5 shows the correlation between the 3D atom-by-atom chemical information of APT with crystallographic characterisation of captured phases and interfaces. The rational interface dataset, previously shown in Fig. 3a, has been further studied here. Fig. 5a shows a reconstruction where only Ni and Mo atoms have been included for clarity. Compositional variation enables the austenite and ferrite to be segmented with isoconcentration surfaces (Fig. 5b). The crystallographic orientation of each austenite and ferrite grain is also determined through a combination of crystallographic information contained directly within the APT data and the correlative EBSD data in the interfacial region acquired prior to lift-out of the specimen. The details of the methodology used is detailed in the *supplementary materials*. This methodology employs sophisticated APT detector mapping approaches as developed in [48]. Fig. 5c shows the resulting inverse pole figure map of the reconstruction. Further, the interface surface is defined through a Delaunay triangulated mesh using a similar approach to that described in [32] and is shown in Fig. 5d. The normal for each mesh component can then be calculated (Fig. 5e), and an average surface ($\bar{n}$) determined. The average surface normal, as defined in the specimen frame of reference (Cs), and the corresponding austenite and ferrite crystal frames of reference (Cc) are provided in Fig. 5f. Both these values show deviation from the $\{111\}_A/\{110\}_F$ habit planes measured from thousands of interfaces in the bulk of the samples (see Fig. 2). This highlights the importance of statistically significant analyses of interfaces, as the atomic resolution analysis of limited segments of only individual boundaries may not be representative of the bulk behaviour. However, our workflow enables an atomic-resolution and complete '5+(n-1)-parameter' characterization of the rational ferrite-austenite

boundary – three parameters to define the 3D disorientation of the grains, two to define the boundary normal direction, and n-1 to define the interfacial elemental excess of a chosen element of interest out of n elements existing within the material.

In summary, this study of the crystallography and composition of austenite-ferrite interphase boundaries finds that they tend to terminate on $\{111\}_A/\{110\}_F$ planes, and this tendency increases for rational interfaces with the K-S orientation relationship. We show that solute segregation is a function of the interface crystallography and the bonding properties of the various solute atoms. While both rational and irrational interfaces show significant segregation of C and N, substitutional elements show a much stronger tendency to segregate to irrational boundaries. A heterogeneous distribution of solute elements in the austenite-ferrite interphase boundary plane is shown, underpinning the complexities associated with correlating properties of interfaces to their crystallography and chemistry. Our findings highlight that a knowledge of misorientation and habit planes (five crystallographic parameters) alone is not sufficient to make meaningful connections to many interface-controlled materials properties in alloys such as duplex stainless steel, and that for an alloy containing n elements, an integrated set of five crystallographic parameters and n-1 chemistry parameters, is crucial for further advancing the microstructure design.

Declaration of competing interest

The authors declare that they have no known competing financial interests or personal relationships that could have appeared to influence the work reported in this paper.

Acknowledgements

Funding from the AUSMURI program administered by the Australia's Department of Industry, Science, Energy and Resources and the Australian Research Council (DP230101063 and DP230100183) is acknowledged. The authors acknowledge the facilities, scientific, and technical support provided at the Electron Microscope Unit, UNSW Sydney (Mark Wainwright Analytical Centre), as well as Sydney Microscopy & Microanalysis (SMM) at the University of Sydney — both nodes of Microscopy Australia, a national research facility supported under the Commonwealth NCRIS program.

Supplementary materials

Supplementary material associated with this article can be found, in the online version, at doi:10.1016/j.scriptamat.2024.116049.

References

[1] N. Haghdadi, M. Laleh, A. Kosari, M.H. Moayed, P. Cizek, P.D. Hodgson, H. Beladi, The effect of phase transformation route on the intergranular corrosion susceptibility of 2205 duplex stainless steel, Mater. Lett. 238 (2019) 26–30.
[2] L. Zhang, Y. Jiang, B. Deng, W. Zhang, J. Xu, J. Li, Effect of aging on the corrosion resistance of 2101 lean duplex stainless steel, Mater. Charact 60 (2009) 1522–1528.
[3] A. Pinol-Juez, A. Iza-Mendia, I. Gutierrez, δ/γ Interface bondary sliding as a mechanism for strain accommodation during hot deformation in a duplex stainless steel, Metallurgical Mater. Trans. A 31 (2000) 1671–1677.
[4] S.B. Kadambi, Interphase Boundary Segregation Engineering, PhD thesis, North Carolina State University, 2020.
[5] T. Watanabe, Grain boundary engineering: historical perspective and future prospects, J. Mater. Sci. 46 (2011) 4095–4115.
[6] C.A. Schuh, K. Lu, Stability of nanocrystalline metals: the role of grain-boundary chemistry and structure, Mrs Bull. 46 (2021) 225–235.
[7] M.A. Gibson, C.A. Schuh, Segregation-induced changes in grain boundary cohesion and embrittlement in binary alloys, Acta Mater. 95 (2015) 145–155.
[8] T. Chookajorn, M.Park Tongjai, C.A. Schuh, Duplex nanocrystalline alloys: entropic nanostructure stabilization and a case study on W–Cr, J. Mater. Res. 30 (2015) 151–163.
[9] M. Laleh, A.E. Hughes, M.Y. Tan, G.S. Rohrer, S. Primig, N. Haghdadi, Grain boundary character distribution in an additively manufactured austenitic stainless steel, Scr. Mater. 192 (2021) 115–119.
[10] S.A. Dregia, P. Wynblatt, Equilibrium segregation and interfacial energy in multicomponent systems, Acta Metallurgica et Materialia 39 (1991) 771–778.
[11] A. Iza-Mendia, A. Pinol-Juez, J.J. Urcola, I. Gutierrez, Microstructural and mechanical behavior of a duplex stainless steel under hot working conditions, Metallurgical and Mater. Trans. A 29 (1998) 2975–2986.
[12] M.C. Marinelli, A. El Bartali, J.W. Signorelli, P. Evrard, V. Aubin, I. Alvarez-Armas, S. Degallaix-Moreuil, Activated slip systems and microcrack path in LCF of a duplex stainless steel, Materials Sci. Eng. A 509 (2009) 81–88.
[13] N. Haghdadi, D. Abou-Ras, P. Cizek, P.D. Hodgson, A.D. Rollett, H. Beladi, Austenite-ferrite interface crystallography dependence of sigma phase precipitation using the five-parameter characterization approach, Mater. Lett. 196 (2017) 264–268.
[14] G.S. Rohrer, D.M. Saylor, B. El Dasher, B.L. Adams, A.D. Rollett, P. Wynblatt, The distribution of internal interfaces in polycrystals, Int. J. Mater. Res. 95 (2021) 197–214.
[15] S.J. Kang, Y.W. Kim, M. Kim, J.M. Zuo, Determination of interfacial atomic structure, misfits and energetics of Ω phase in Al–Cu–Mg–Ag alloy, Acta Mater. 81 (2014) 501–511.
[16] C.M. Barr, S.M. Foiles, M. Alkayyali, Y. Mahmood, P.M. Price, D.P. Adams, B. L. Boyce, F. Abdeljawad, K. Hattar, The role of grain boundary character in solute segregation and thermal stability of nanocrystalline Pt–Au, Nanoscale 13 (2021) 3552–3563.
[17] R. Kirchheim, Grain coarsening inhibited by solute segregation, Acta Mater. 50 (2002) 413–419.
[18] C. White, C. Liu, R. Padgett, S. Yalisove, Surface and grain boundary segregation in relation to intergranular fracture: boron and sulfur in Ni3Al, Scr. Metal. 18 (1984) 1417–1420.
[19] M. Kuzmina, D. Ponge, D. Raabe, Grain boundary segregation engineering and austenite reversion turn embrittlement into toughness: example of a 9 wt.% medium Mn steel, Acta Mater 86 (2015) 182–192.
[20] K. Babinsky, R. De Kloe, H. Clemens, S. Primig, A novel approach for site-specific atom probe specimen preparation by focused ion beam and transmission electron backscatter diffraction, Ultramicroscopy 144 (2014) 9–18.
[21] M. Herbig, M. Kuzmina, C. Haase, R.K. Marceau, I. Gutiérrez-Urrutia, D. Haley, D. A. Molodov, P. Choi, D. Raabe, Grain boundary segregation in Fe–Mn–C twinning-induced plasticity steels studied by correlative electron backscatter diffraction and atom probe tomography, Acta Mater. 83 (2015) 37–47.
[22] A. Stoffers, O. Cojocaru-Mirédin, W. Seifert, S. Zaefferer, S. Riepe, D. Raabe, Grain boundary segregation in multicrystalline silicon: correlative characterization by EBSD, EBIC, and atom probe tomography, Prog. Photovoltaics: Res. Appl. 23 (2015) 1742–1753.
[23] G. Miyamoto, A. Goto, N. Takayama, T. Furuhara, Three-dimensional atom probe analysis of boron segregation at austenite grain boundary in a low carbon steel-Effects of boundary misorientation and quenching temperature, Scr. Mater. 154 (2018) 168–171.
[24] R. Francis, G. Byrne, Duplex stainless steels—Alloys for the 21st century, Metals (Basel) 11 (2021) 836.
[25] N. Haghdadi, C. Ledermueller, H. Chen, Z. Chen, Q. Liu, X. Li, G.S. Rohrer, X. Liao, S. Ringer, S. Primig, Evolution of microstructure and mechanical properties in 2205 duplex stainless steels during additive manufacturing and heat treatment, Mater. Sci. Eng. A 835 (2022) 142695.
[26] M. Laleh, N. Haghdadi, A.E. Hughes, S. Primig, M.Y. Tan, Enhancing the repassivation ability and localised corrosion resistance of an additively manufactured duplex stainless steel by post-processing heat treatment, Corros. Sci. 198 (2022) 110106.
[27] N. Haghdadi, H. Chen, Z. Chen, S.S. Babu, X.Z. Liao, S.P. Ringer, S. Primig, Intergranular precipitation and chemical fluctuations in an additively manufactured 2205 duplex stainless steel, Scr. Mater. 219 (2022) 114894.
[28] N. Haghdadi, M. Laleh, H. Chen, Z. Chen, Z. Ledermueller, C. Liao, X. Ringer, S, Primig, On the pitting corrosion of 2205 duplex stainless steel produced by laser powder bed fusion additive manufacturing in the as-built and post-processed conditions, Mater. Des. 212 (2021) 110260.
[29] D. Zhang, A. Liu, B. Yin, P. Wen, Additive manufacturing of duplex stainless steels-a critical review, J. Manuf. Process 73 (2022) 496–517.
[30] F. Hengsbach, P. Koppa, K. Duschik, M.J. Holzweissig, M. Burns, J. Nellesen, W. Tillmann, T. Tröster, K.P. Hoyer, M. Schaper, Duplex stainless steel fabricated by selective laser melting-Microstructural and mechanical properties, Mater. Des. 133 (2017) 136–142.
[31] Atom-Probe-Toolbox/voltageCurveMC.m At Master · Peterfelfer/Atom-Probe-Toolbox, GitHub, 2023. https://github.com/peterfelfer/Atom-Probe-Toolbox. Accessed June 2023.
[32] P. Felfer, B. Scherrer, J. Demeulemeester, W. Vandervorst, J.M. Cairney, Mapping interfacial excess in atom probe data, Ultramicroscopy 159 (2015) 438–444.
[33] H.K.D.H. Bhadeshia, Bainite Steels, Inst. Metals (1992).
[34] G. Miyamoto, K. Yokoyama, T. Furuhara, Quantitative analysis of Mo solute drag effect on ferrite and bainite transformations in Fe-0.4 C-0.5 Mo alloy, Acta Mater. 177 (2019) 187–197.
[35] G. Brückner, J. Pospiech, I. Seidl, G. Gottstein, Orientation correlation during diffusional α→ γ phase transformation in a ferritic low carbon steel, Scr. Mater. 44 (2001) 2635–2640.
[36] J.W. Cahn, J.E. Hilliard, Free energy of a nonuniform system. I. Interfacial free energy, J. Chem. Phys. 28 (1958) 258–267.
[37] Y.W. Lee, H.I. Aaronson, Anisotropy of coherent interphase boundary energy, Acta Metallurgica 28 (1980) 539–548.

[38] O. Thuillier, F. Danoix, M. Gouné, D. Blavette, Atom probe tomography of the austenite–ferrite interphase boundary composition in a model alloy Fe–C–Mn, Scr. Mater. 55 (2006) 1071–1074.
[39] Z. Xiao, L. He, X.M. Bai, First principle studies of effects of solute segregation on grain boundary strength in Ni-based alloys, J Alloys Compd. 874 (2021) 159795.
[40] H. Dong, Y. Zhang, G. Miyamoto, M. Inomoto, H. Chen, Z. Yang, T. Furuhara, Unraveling the effects of Nb interface segregation on ferrite transformation kinetics in low carbon steels, Acta Mater. 215 (2021) 117081.
[41] G. Miyamoto, T. Furuhara, Interaction of alloying elements with migrating ferrite/austenite interface, Isij Intl. 60 (2020) 2942–2953.
[42] L. Li, R.D. Kamachali, Z. Li, Z. Zhang, Grain boundary energy effect on grain boundary segregation in an equiatomic high-entropy alloy, Phys. Rev. Mater. 4 (2020) 053603.
[43] R. Kirchheim, Reducing grain boundary, dislocation line and vacancy formation energies by solute segregation. I. Theoretical background, Acta Mater. 55 (2007) 5129.
[44] B. Wu, Z. Wang, C. Shang, Y. Yu, C.Z. Z.Yang, A route to produce toughened acicular ferrite with equivalent hardness as martensite: the combined effect of elements segregation and pre-transformed allotriomorphic ferrite, Mate.r Charact. 182 (2021) 111528.
[45] F. Danoix, X. Sauvage, D. Huin, L. Germain, M. Gouné, A direct evidence of solute interactions with a moving ferrite/austenite interface in a model Fe-C-Mn alloy, Scr. Mater. 121 (2016) 61–65.
[46] H. Jin, I. Elfimov, M. Militzer, First-principles simulations of binding energies of alloying elements to the ferrite-austenite interface in iron, J. Appl. Phys. 123 (2018) 085303.
[47] B.W. Krakauer, D.N. Seidman, Absolute atomic-scale measurements of the Gibbsian interfacial excess of solute at internal interfaces, Phys. Rev. B 48 (1993) 6724.
[48] A.J. Breen, A.C. Day, B. Lim, W.J. Davids, S.P. Ringer, Revealing latent pole and zone line information in atom probe detector maps using crystallographically correlated metrics, Ultramicroscopy 243 (2023) 113640.